THESIS FOR THE DEGREE OF LICENTIATE OF ENGINEERING

Reconfigurable Intelligent Surfaces for Over-the-Air Testing of Wireless Systems

Yuqing Zhu

CHALMERS
UNIVERSITY OF TECHNOLOGY

Department of Electrical Engineering
Chalmers University of Technology
Gothenburg, Sweden, 2025

Reconfigurable Intelligent Surfaces for Over-the-Air Testing of Wireless Systems

Yuqing Zhu

Department of Electrical Engineering
Chalmers University of Technology
SE-412 96 Gothenburg, Sweden
Phone: +46 (0)31 772 1000
www.chalmers.se

Printed by Chalmers Reproservice
Gothenburg, Sweden, August 2025

To the ceaseless quest.

Abstract

Extensive research into reconfigurable intelligent surface (RIS) technology for manipulating electromagnetic (EM) propagation environments has enabled a wide range of emerging applications. This thesis explores the application of RISs in developing efficient and cost-effective over-the-air (OTA) testing methods and platforms for future wireless systems—a use case that demands advanced RIS architectures capable of complex field synthesis. Departing from conventional phase-only RIS designs, this work focuses on the development of amplitude-phase controllable RISs to provide enhanced control flexibility. A comprehensive framework encompassing RIS unit cell (UC) design, modeling, analysis, and experimental validation is established, addressing key technical challenges encountered at millimeter-wave (mmWave) frequencies.

This study presents a complete workflow from component-level evaluation to system-level demonstration. Tunable components—specifically *p-i-n* and varactor diodes—are experimentally characterized, and improved diode circuit models (DCMs) and EM models (EMMs) are developed to capture high-frequency parasitics and bias-dependent junction impedances. Two mmWave UCs are designed to address device-specific constraints: the varactor-based UC achieves continuous phase tuning exceeding 330.7°, despite a limited capacitance tuning ratio of 1.8; the *p-i-n*-based UC enables continuous amplitude tuning from 0 to 0.8, while revealing distinct nonlinear phase shift.

To realize simultaneous, independent, and continuous amplitude-phase control, a loop-embedded, end-folded RIS UC is proposed, integrating a forward-biased *p-i-n* diode and a reverse-biased varactor diode. A generalized complex-plane representation, referred to as Γ-coverage, is introduced to visualize UC reflection properties across the full bias space. Two performance metrics, A_{cov} and $\Gamma_{\max}$, are defined to quantify reconfigurability. At 28 GHz, the UC achieves a 0–0.5 amplitude tuning range and full 360° phase control, with maximized Γ-coverage. The design employs a rigorous EM-circuit co-design methodology, incorporating DCMs, EMMs, and a semi-analytical equivalent circuit model (ECM) for accurate performance prediction under varying bias conditions and incidence angles.

The proposed RIS UC is further validated in a proof-of-concept OTA scenario, serving as a near-field plane wave (PW) generator for a compact antenna test range (CATR). The RIS-assisted configuration demonstrates high field uniformity and over 20 dB improvement in dynamic range compared to

conventional far-field test ranges. These results highlight the strong potential of RIS technology for integration into next-generation OTA testing platforms.

Keywords: Reconfigurable intelligent surface (RIS), millimeter-wave (mmWave), amplitude and phase control, over-the-air (OTA) testing.

List of Publications

This thesis is based on the following publications:

[A] **Y. Zhu**, A. R. Vilenskiy, O. A. Iupikov, P. S. Krasov, T. Emanuelsson, G. Lasser, M. V. Ivashina, "A varactor-based reconfigurable intelligent surface concept for 5G/6G mm-wave applications". *2024 18th European Conference on Antennas and Propagation (EuCAP)*, Glasgow, United Kingdom, pp. 1–5, 2024.

[B] **Y. Zhu**, A. Vilenskiy, O. Iupikov, P. Krasov, T. Emanuelsson, G. Lasser, M. Ivashina, "Improved equivalent circuit model of p-i-n diodes for amplitude and phase controllable mmWave reconfigurable intelligent surfaces". *2024 IEEE International Symposium on Antennas and Propagation and INC/USNC-URSI Radio Science Meeting (AP-S/INC-USNC-URSI)*, Firenze, Italy, pp. 1583–1584, 2024.

[C] **Y. Zhu**, A. R. Vilenskiy, O. A. Iupikov, P. S. Krasov, T. Emanuelsson, G. Lasser, M. V. Ivashina, "Millimeter-wave reconfigurable intelligent surface with independent and continuous amplitude-phase control: Unit cell design and circuit model". *IEEE Transactions on Antennas and Propagation*, early access.

Other publications by the author, not included in this thesis, are:

[D] O. A. Iupikov, A. R. Vilenskiy, **Y. Zhu**, P. S. Krasov, M. V. Ivashina, "Reconfigurable intelligent surfaces for OTA testing: Optimization and initial results". *2023 IEEE Conference on Antenna Measurements and Applications (CAMA)*, Genoa, Italy, pp. 846–851, 2023.

[E] A. Tabeshnezhad, **Y. Zhu**, A. Vilenskiy, V. Ly Nguyen, A. Lee Swindlehurst, T. Svensson, "Jammer mitigation in absorptive RIS-assisted uplink NOMA". *arXiv:2408.16786*, 2024.

[F] P. S. Krasov, O. A. Iupikov, A. R. Vilenskiy, **Y. Zhu**, M. V. Ivashina, "Reconfigurable intelligent surfaces for OTA testing: Wireless cable". *2024 54th European Microwave Conference (EuMC)*, Paris, France, pp. 232–235, 2024.

[G] P. S. Krasov, O. A. Iupikov, A. Vilenskiy, **Y. Zhu**, T. Emanuelsson, G. Lasser, R. Maaskant, J. Friden, M. V. Ivashina, "Innovative hybrid RC-AC test environments and RIS-enabled plane wave generation". *2024 Antenna Measurement Techniques Association Symposium (AMTA)*, Cincinnati, OH, USA, pp. 1–6, 2024.

[H] I. Shilinkov, O. Iupikov, P. Krasov, **Y. Zhu**, R. Maaskant, M. Ivashina, "Measurement of reconfigurable intelligent surfaces through the back-scattering method: Demonstration at 28 GHz". *2025 19th European Conference on Antennas and Propagation (EuCAP)*, Stockholm, Sweden, pp. 1–4, 2025.

[I] P. S. Krasov, O. A. Iupikov, A. R. Vilenskiy, **Y. Zhu**, M. V. Ivashina, "RIS with continuous amplitude and phase control: Functional testing method and implementation". *2025 19th European Conference on Antennas and Propagation (EuCAP)*, Stockholm, Sweden, pp. 1–5, 2025.

[J] P. S. Krasov, O. A. Iupikov, **Y. Zhu**, M. V. Ivashina, "The choice of time gating parameters for characterization of the reconfigurable intelligent surfaces with continuous amplitude and phase control". *2025 55th European Microwave Conference (EuMC)*, Utrecht, The Netherlands, accepted.

Acknowledgments

The research presented in this thesis would not have been possible without the unwavering support and invaluable contributions of numerous individuals, to whom I extend my deepest gratitude.

Foremost, I express my profound appreciation to my main supervisor, Marianna Ivashina, for her exceptional guidance, timely assistance, and steadfast encouragement throughout my research journey. Her expertise and mentorship were indispensable to the successful completion of this work.

Special thanks are also due to my co-supervisors: Artem Vilenskiy, Oleg Iupikov, and Pavlo Krasov (Department of Electrical Engineering); Gregor Lasser (Department of Microtechnology and Nanoscience); and my industrial supervisor, Thomas Emanuelsson (Ericsson). Their insightful feedback, technical expertise, and genuine inspiration greatly enriched my research and academic development.

Furthermore, I wish to express my sincere gratitude to my examiner, Erik Ström, for his pivotal guidance in project execution and consistent support in advancing the research trajectory.

I am genuinely grateful to the professors, colleagues, and friends in the Antenna System Group for their collaborative spirit, technical support, and stimulating discussions. The vibrant exchange of ideas and supportive environment made this research experience exceptionally rewarding.

I also acknowledge the financial support from the OTA5G+ Project (funded by Rohde & Schwarz, Ericsson, Icomera, Bluetest, and Chalmers at the GigaHertz-ChaseOn Bridge Centre) and the AutOTA Project (funded by Vinnova, Ericsson, Volvo Cars, RISE, Icomera, and UniqueSec at the WiTECH Centre). My sincere thanks extend to all industrial partners for their collaborative engagement and fruitful discussions.

Finally, my heartfelt gratitude goes to my family and friends for their unwavering encouragement, dedication, and boundless support. Their belief in me has been a constant source of strength throughout this journey. I also cherish the goodwill and kindness I encountered along the way.

Acronyms

RIS:	Reconfigurable intelligent surface
OTA:	Over-the-air
UC:	Unit cell
Γ:	Reflection coefficient
mmWave:	Millimeter-wave
EM:	Electromagnetic
DCM:	Diode circuit model
EMM:	Electromagnetic model
ECM:	Equivalent circuit model
GCPW:	Grounded coplanar waveguide
TRL:	Through-reflect-line
PW:	Plane wave
DUT:	Device under test
CATR:	Compact antenna test range

Contents

Part I

Overview

CHAPTER 1

Introduction

1.1 RIS and Emerging OTA Testing Applications

Reconfigurable intelligent surfaces (RISs) are envisioned as a promising technology for transforming the inherently implicit and random wireless propagation environment into a programmable and controllable one by tailoring the electromagnetic (EM) wavefront of incident radio signals [1]. An RIS typically consists of a large number of individually tunable unit cells (UCs), whose microscopic design collectively determines the macroscopic response of the surface. This EM wave manipulation capability enables a variety of potential applications, including non-line-of-sight coverage enhancement, interference suppression, and beam focusing for radio localization and wireless power transfer, contributing to the realization of smart radio environments, as illustrated in Fig. 1.1.

While RISs have been extensively studied for enhancing wireless communication systems, their applicability extends further into other novel domains. One notable emerging near-field application is RIS-assisted over-the-air (OTA) testing of wireless systems, as elaborated in Papers [D], [F], and [G]. In this context, RISs are employed to synthesize reconfigurable channel matrices,

Figure 1.1: RIS-enabled smart radio environments [1].

enabling dynamic test environments for devices under test (DUTs). This approach offers a cost-effective alternative to large-scale active phased arrays and multi-probe compact antenna test ranges (CATRs), particularly at millimeter-wave (mmWave) frequencies. Representative OTA testing scenarios include plane wave (PW) generation with controllable angles of arrival to emulate the test zone volume (see Paper [D]), as well as the emulation of a wireless cable environment that links test probes and DUTs with high channel isolation (see Paper [F]), as sketched in Fig. 1.2.

The expanding application to OTA testing imposes more stringent requirements on the functionality of RISs. Traditional phase-only controllable RIS architectures, typically limited to 1-bit or 2-bit resolution, are insufficient for accurately shaping the field distribution [2]. To meet the accuracy demands of the above configurations, RISs must support advanced field synthesis algorithms that utilize simultaneous amplitude-phase control across the reflection-absorption spectrum. This necessitates the development of optimized RIS UCs with high-resolution biasing, while accounting for amplitude-phase interdependence. The specific UC requirements needed to achieve the desired OTA chamber quality are summarized in Table 1.1.

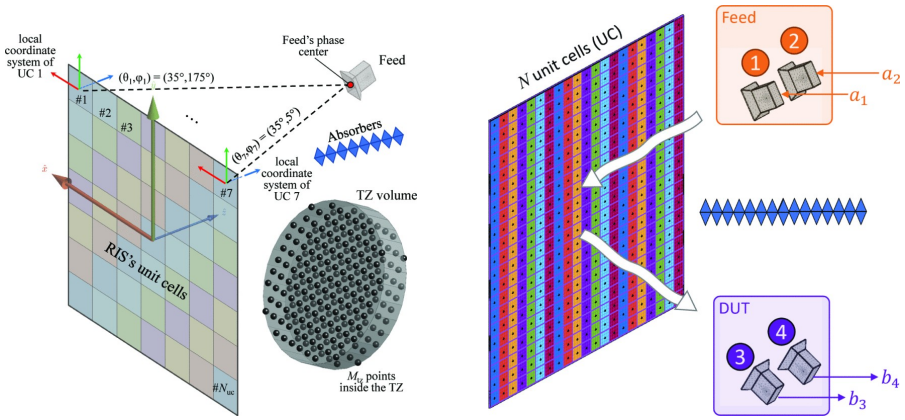

(a) (b)

Figure 1.2: Examples of RIS-assisted OTA testing systems. (a) PW generator [D]. (b) Wireless cable [F].

Table 1.1: Requirements for the RIS UC in OTA Testing Applications

Requirements	PW generator [D]	Wireless cable [F]
Independent amplitude-phase control	Yes	Yes
Amplitude and phase resolution	≥4 bits	≥5 bits
Amplitude dynamic range	≥23 dB	≥16 dB
Phase dynamic range	360°	360°

1.2 Amplitude-Phase Controllable RISs

Compared to conventional phase-only control methods [3], achieving full amplitude-phase reconfigurability in RISs remains largely unexplored. In recent years, reflective RISs and reconfigurable metasurfaces with real-time, simultaneous amplitude and phase tuning have garnered growing attention. Various reconfigurable mechanisms have been investigated, including discrete diode films [4]–[11], graphene [12], [13], vanadium dioxide [14], and integrated circuits [15]. Several reported solutions are shown in Fig. 1.3. These developments have opened up new avenues for multifunctional RIS applications, particularly in flexible beamforming scenarios such as multi-beam steering

with variable power intensity.

Among these approaches, diode-integrated UCs are widely adopted due to their relatively low complexity and cost. For instance, *p-i-n* diodes can be switched between ON and OFF states to realize 1-bit phase quantization [4], or biased in transition states for amplitude control [5], [6]. However, in such designs, amplitude and phase cannot be controlled independently, resulting in a limited set of discrete UC states [7], [8].

Continuous amplitude-phase control has been demonstrated using configurations such as dual varactor diodes for arbitrary state combinations [9], or separate coupled resonators [10]. Nevertheless, both approaches suffer from limited amplitude-phase tuning ranges, thereby constraining the achievable control accuracy. Although cascading programmable reflection-type attenuators and phase shifters can provide full phase coverage [11], the resulting multi-layer topology involving six diodes per UC poses significant complexity and integration limitations.

1.3 Challenges in RIS Research Area

Design challenges Despite the aforementioned amplitude-phase reconfigurable designs [4]–[11], most implementations are limited to operation below 10 GHz, while RISs at mmWave frequencies (e.g., K_a-band) are seldom reported. Designing UCs for mmWave bands involves more than mere frequency scaling from lower bands; rather, it presents significant challenges due to the pronounced parasitic effects of tunable components and increased losses stemming from materials and fabrication processes. As a result, even phase-only mmWave RIS designs remain relatively rare in the literature[16]–[18].

Furthermore, achieving simultaneous and independent amplitude-phase control, particularly when both reflection and absorption states are considered, adds substantial complexity to the UC design process. Determining an optimal UC geometry becomes non-intuitive, and the associated biasing circuitry increases in complexity. These challenges are further exacerbated when high control accuracy, such as multi-bit resolution or continuous tuning, is required.

Technological challenges The performance of RISs is closely tied to the characteristics of tunable components such as *p-i-n* and varactor diodes. However, their availability at mmWave frequencies is limited. As frequency in-

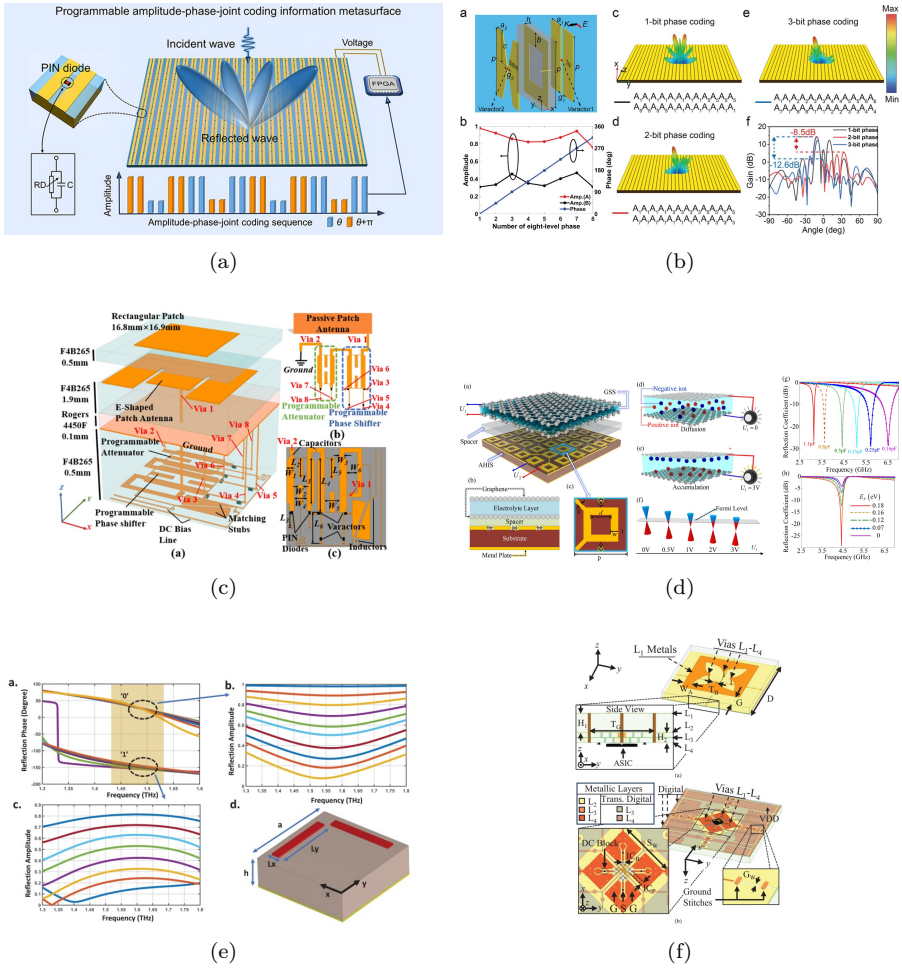

(a) (b) (c) (d) (e) (f)

Figure 1.3: Reported amplitude-phase controllable RISs or metasurfaces. (a) Diode-based continuous amplitude and 1-bit phase control [5]. (b) Diode-based 1-bit amplitude and 3-bit phase control [8]. (c) Diode-based continuous amplitude-phase control [11]. (d) Graphene- and diode-based continuous amplitude-phase control [12]. (e) Vanadium dioxide-based continuous amplitude and 1-bit phase control [14]. (f) Integrated circuit-based continuous amplitude-phase control [15].

creases into the K_a-band, the number of commercially available diodes with packaging suitable for high-frequency integration (e.g., flip-chip) decreases significantly [19].

Moreover, parasitic and nonlinear effects become more pronounced at higher frequencies, degrading the quality factor of these devices. This is particularly problematic for varactor diodes, whose capacitance tuning range diminishes rapidly with increasing frequency, thereby constraining the achievable phase tuning range of UCs that strongly depend on this factor. These inherent limitations significantly hinder the realization of wide-range amplitude-phase tuning in practical UC designs.

Modeling challenges Accurate modeling of both tunable diodes and UCs is essential in the RIS design process. However, the scarcity of mmWave RIS implementations implies that existing modeling approaches remain largely unvalidated in this frequency regime.

On one hand, the limited availability of high-frequency tunable electronics restricts the development of corresponding circuit models. While simplified diode circuit models (DCMs) may suffice for phase-only control or low-frequency scenarios, they become inadequate for amplitude-phase controllable mmWave UCs. In such cases, DCMs must account for both high-frequency parasitic effects and nonlinear junction behavior under continuous bias conditions, making accurate diode measurement and characterization indispensable.

On the other hand, although full-wave EM simulations are the primary tool for UC design, simplified physics-based approaches, such as equivalent circuit models (ECMs), are valuable for gaining operational insight and enabling time-efficient analysis. Furthermore, tractable ECMs that effectively capture the physical behavior of RISs are particularly useful for accurate system-level simulation and channel estimation in wireless communication research, as demonstrated in the collaborative study in Paper [E]. However, for UCs with irregular geometries, where explicit current distributions are not readily obtainable [20], [21], ECMs often suffer from reduced accuracy when predicting performance variations with frequency, incidence angle, and bias state.

Analysis challenges The reflective behavior of a UC is typically characterized by its complex reflection coefficient (Γ). Traditional analysis methods evaluate reconfigurability by plotting amplitude and phase responses separately

in Cartesian form, using multiple curves or colormaps [11], [15]. However, such representations fail to intuitively convey the coupling or independence between amplitude and phase, especially when involving a wide range of tunable states.

Consequently, there remains a lack of generalized and informative representation approaches for visualizing UC performance, as well as suitable performance metrics capable of quantifying reconfigurability while accounting for the inherent interdependence of amplitude and phase control. These limitations hinder effective UC biasing, optimization, and benchmarking across different designs.

These multifaceted challenges underscore the need for a unified framework that not only enables accurate modeling and design of mmWave RIS UCs, but also facilitates efficient performance evaluation and optimization.

1.4 Scientific Contributions

This thesis addresses critical challenges in the design, modeling, and analysis of mmWave RIS UCs for OTA testing applications, and makes the following key scientific contributions:

Advanced mmWave UC design and application validation Proposes a RIS UC integrating *p-i-n* and varactor diodes tailored for mmWave frequencies, accounting for critical diode parasitic effects and PCB-related losses. The UC enables independent and continuous amplitude-phase control, supporting a full 360° phase tuning range. The design demonstrates strong potential for RIS-assisted OTA testing applications, with an exemplary near-field PW generation scenario that proves high field uniformity and significant dynamic range enhancement compared to conventional far-field test ranges.

Tunable component characterization and evaluation Investigates and experimentally characterizes tunable components, including *p-i-n* and varactor diodes, for mmWave operation. Separate mmWave RIS UCs are developed to evaluate and address component limitations, achieving continuous phase control with improved phase coverage despite a limited capacitance tuning ratio, as well as continuous amplitude control with 1-bit phase resolution that

accounts for diode transition states.

Comprehensive EM-circuit modeling framework Adopts a combined EM-circuit design framework integrating numerical EM data with empirical diode data across all bias states. Improved DCMs and EM models (EMMs) for both diode types are formulated for continuous biasing, incorporating high-frequency parasitic effects and nonlinear junction behavior. A semi-analytical ECM of the UC, combining Floquet modal expansion and lumped component modeling, is derived to enhance accuracy across varying incident angles and validated for diode-loaded, complex-shaped UC geometries.

Generalized representation and performance metrics Introduces a generalized representation of UC reflection properties, termed Γ-coverage, which maps both amplitude and phase of Γ on the complex plane over a continuous range of bias states. Alongside, new performance metrics (A_{cov} and Γ_{max}) are proposed to quantitatively assess reconfigurability. This approach facilitates intuitive analysis of independent amplitude-phase tuning and guides the selection of optimal bias states.

1.5 Thesis Outline

This thesis begins with an introduction outlining the motivation and challenges of amplitude-phase controllable mmWave RISs for OTA testing of wireless devices (Chapter 1). It then details the foundational principles for implementing amplitude-phase reconfigurability, including the characterization of tunable components (Chapter 2). This is followed by an in-depth presentation of UC design, modeling, analysis, and measurement aimed at achieving independent and continuous amplitude-phase control (Chapter 3). The proposed RIS is applied in OTA testing scenarios, showcasing notable performance benefits (Chapter 4). A summary of the included scientific papers highlights the core contributions (Chapter 5). Finally, the thesis concludes with closing remarks and perspectives on future research directions (Chapter 6).

CHAPTER 2

Implementation Basis for Amplitude-Phase Control

This chapter establishes the foundational implementation for amplitude-phase controllable RISs. Two control schemes are demonstrated: phase control using a varactor diode, and amplitude-phase control employing a *p-i-n* diode. Diode modeling and measurements across continuous bias states are conducted. Section 2.1 is based on the contributions of Paper [A], while Sections 2.2 and 2.3 draw on the results presented in Paper [B].

2.1 Varactor-Based Continuous Phase Control

This section presents a 28 GHz varactor-based RIS UC designed to overcome the phase shift range limitations typically observed at mmWave frequencies. A 3-bit phase quantization example ($\geq 315^\circ$ phase coverage) is demonstrated. As shown in Fig. 2.1, the proposed UC (denoted as UC 4) features a split radiating patch on a back-shielded dielectric substrate, enclosed by a grounded square loop. A reverse-biased varactor diode bridges the patch halves to enable tunable phase shifts. The UC is arranged on a periodic $0.28\lambda_0$ square lattice.

A four-step evolution process reveals the design rationale. Starting with a symmetric slotted patch (UC 1), the phase tuning range is enhanced by intro-

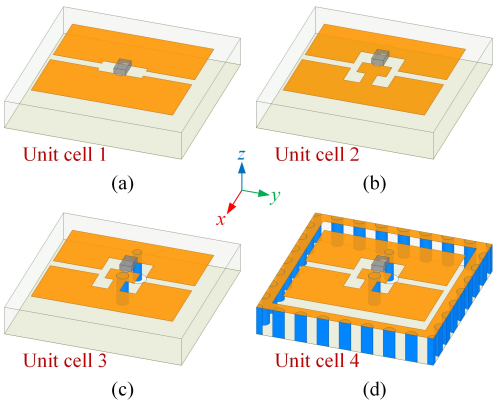

Figure 2.1: Geometry and design evolution of the varactor-based mmWave UC. (a) UC 1. (b) UC 2. (c) UC 3. (d) UC 4.

ducing asymmetry via an offset diode position (UC 2). UC 3 adds grounded and bias vias for DC control, which simultaneously act as shunt inductors to further increase phase coverage. The final UC 4 integrates a grounded square loop forming a substrate-integrated cavity, which adjusts the inter-element coupling capacitance to achieve wideband, large phase coverage. The via fences also reduce angular sensitivity.

Fig. 2.2 compares the achievable phase coverage across different UC designs. The varactor diode (MAVR-000120-14110G) is modeled using total equivalent capacitance incorporating parasitic effects at mmWave frequencies, with a total capacitance tuning ratio $C_{\max}/C_{\min} = 1.8$ under a reverse DC voltage range from -12 V to 0 V. With this limited tuning ratio, the baseline symmetric UC 1 yields only 200.5° phase coverage. Introducing asymmetry in UC 2 increases coverage by 80°, although the center frequency shifts downward from 30.7 GHz to 24.8 GHz due to an extended current path. Adding a grounded via in UC 3 compensates for this frequency shift and further expands the phase coverage, yet still falls short of the 3-bit quantization requirement. The proposed UC 4 overcomes this limitation, achieving a phase tuning range over 315° within 26.37–29.61 GHz (about 11.6%), with a maximum value of 330.7°. Note that the geometry modifications also increase the quality factor, steepening the phase-frequency slope. Thus, a balanced trade-off is necessary among phase range, reflection loss, and voltage control capability to ensure

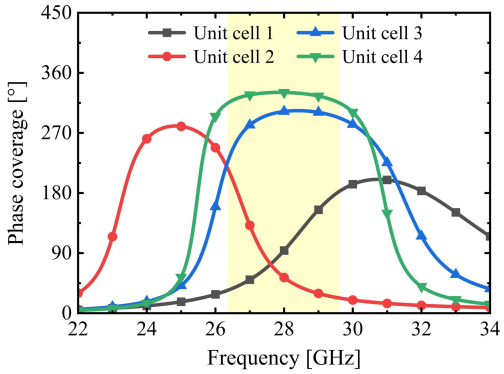

Figure 2.2: Simulated phase coverage of each UC design.

both performance and feasibility.

2.2 Diode Modeling and Measurements

The preceding example uses simplified diode models to highlight performance limitations at high frequencies and to guide key design considerations. However, accurate diode modeling is essential for reliable evaluation of RIS performance. This section presents improved DCMs for both *p-i-n* and varactor diodes, with empirical parameters extracted from experimental characterization to support amplitude-phase controllable UC design.

At mmWave frequencies, diode models must capture parasitic effects and continuous bias-dependent junction behavior. This is particularly important for *p-i-n* diodes, which operate not only in conventional ON/OFF states but also in intermediate transition states between zero bias and full conduction. The proposed DCMs are illustrated in Fig. 2.3. For the *p-i-n* diode, the junction is modeled by a variable resistance R_j and a variable diffusion capacitance C_j in parallel, both controlled by the forward bias current I_f. The capacitance accounts for carrier distribution changes across the junction, which significantly affect behavior at mmWave frequencies. For the varactor diode, the junction is represented by a variable capacitance controlled by the reverse bias voltage U_r. Both models are de-embedded to the diode pads and include intrinsic parasitics as well as pad- and substrate-related effects, including series

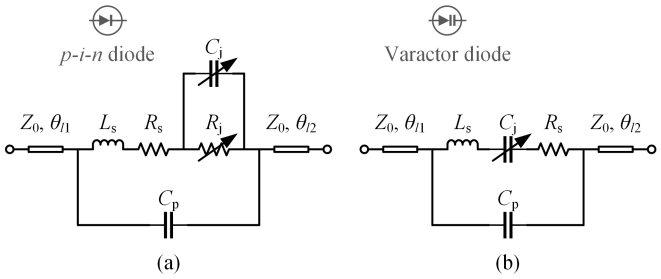

Figure 2.3: Proposed circuit models of diodes. (a) *p-i-n* diode. (b) Varactor diode.

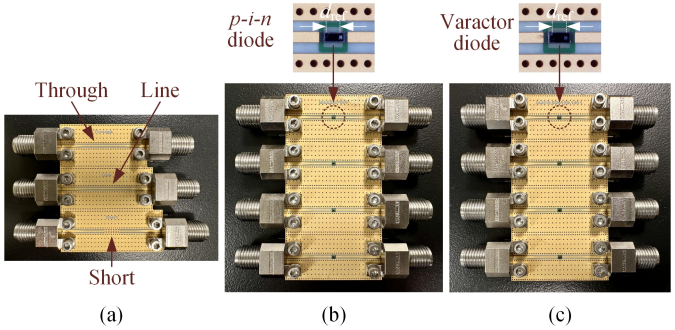

Figure 2.4: Experimental setup for diode characterization. (a) TRL GCPW calibration kit. (b) *p-i-n* diode samples. (c) Varactor diode samples.

inductance L_s, contact resistance R_s, and parallel capacitance C_p representing packaging and edge pad capacitance. Additionally, two ideal transmission lines with characteristic impedance Z_0 and electrical lengths θ_{l1} and θ_{l2} are added to the anode and cathode, respectively, to model time delay caused by physical diode and pad lengths, which becomes non-negligible at mmWave frequencies. The asymmetry in junction location leads to unequal θ_{l1} and θ_{l2}.

Experimental validation of the proposed DCMs is carried out using MADP-000907-14020W *p-i-n* diodes and MAVR-000120-14110G varactor diodes. As shown in Fig. 2.4, each diode is mounted in a two-port series configuration on 75 Ω grounded coplanar waveguides (GCPWs). Repeated measurements on identical samples ensure consistency. A through-reflect-line (TRL) calibration kit is employed to de-embed measurement references to the diode pad edges.

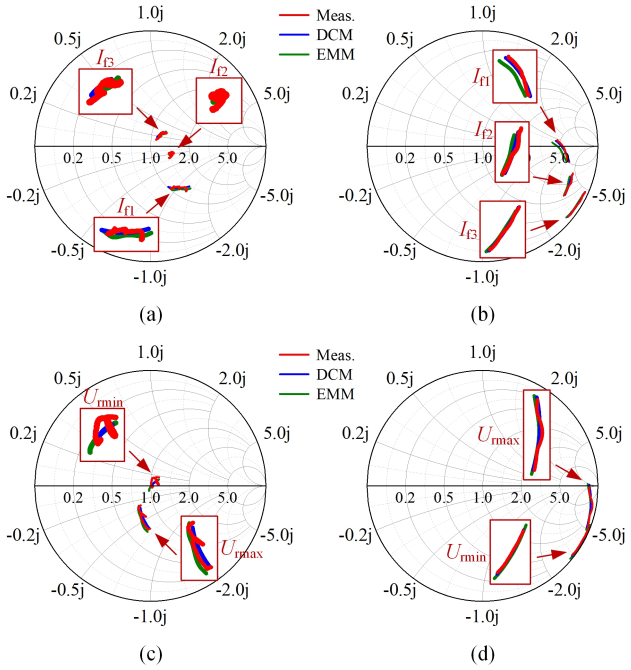

Figure 2.5: S-parameters of p-i-n and varactor diodes over 20–32 GHz from measurements, DCMs, and EMMs, plotted on the Smith chart. (a) S_{11} and (b) S_{21} of p-i-n diodes. (c) S_{11} and (d) S_{21} of varactor diodes.

Stepped DC biases (I_f or U_r) are applied via a bias tee connected to the vector network analyzer, and S-parameters are measured across the 20–32 GHz band under all bias conditions.

Both variable junction parameters and fixed parameters are extracted by fitting the measured S-parameters. These empirical values remain valid across frequencies, bias states, and diode samples. Fig. 2.5 compares circuit-level simulated and measured results under various bias conditions. Additionally, simulations of the 3D EM structures in Fig. 2.4, comprising EMMs of both diodes, are provided. Each EMM preserves key geometric features to accurately capture intrinsic parasitics and includes diode pads. Junction effects are modeled by lumped RLC boundaries with bias-dependent R_j or C_j, inserted differentially into the signal line gap. These EMMs facilitate full-wave UC

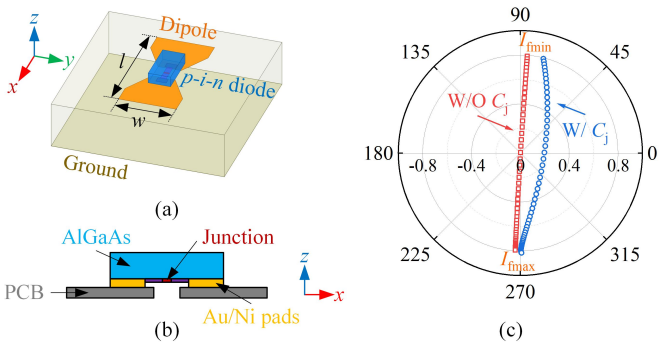

Figure 2.6: Geometry and simulation results of the *p-i-n*-based mmWave UC. (a) Front view of the UC. (b) Schematic of the EMM. (c) Simulated Γ with and without C_j on the complex plane at 28 GHz.

simulation by accounting for interactions between the diode and its surrounding environment. The close agreement between simulations and measurements verifies the accuracy and generality of the proposed models.

2.3 *p-i-n*-Based Continuous Amplitude Control

To evaluate the impact of the improved *p-i-n* DCM, this section presents a mmWave RIS UC integrating a single *p-i-n* diode for continuous amplitude control, as shown in Fig. 2.6. The UC consists of a simple dipole printed on a grounded dielectric slab. Simulated Γ for various I_f are analyzed, comparing cases with and without C_j.

The UC achieves a phase coverage of approximately 180° (i.e., 1-bit phase resolution) and amplitude variation from 0 to 0.8. Notably, the presence of C_j in the transition state introduces additional phase shifts, causing Γ points to deviate from a straight line on the complex plane. This effect also induces observable frequency shifts.

These results highlight the importance of incorporating diode junction effects in *p-i-n*-enabled amplitude-tuning mmWave RIS designs, where nonlinear behavior associated with bias-dependent C_j provides critical insight into reflection field control.

CHAPTER 3

Independent and Continuous Amplitude-Phase Control

In this chapter, a mmWave RIS UC with independent and continuous amplitude-phase control is presented. A generalized complex-plane representation, termed Γ-coverage, is introduced alongside new performance metrics to evaluate the UC's reconfigurability. The design is analyzed using both EM and circuit-level approaches, and is experimentally validated through a waveguide simulator. This chapter is based on the contributions of Paper [C].

3.1 RIS UC Configuration

The proposed amplitude-phase controllable RIS UC, illustrated in Fig. 3.1, adopts a square lattice with a period of $0.42\lambda_0$ at 28 GHz. It comprises two stacked laminates (Sub.1 and Sub.2), bonded with a prepreg layer and featuring four copper layers. where Sub.1 hosts the scattering structure, while Sub.2 supports the bias circuitry.

A segmented, end-folded patch is printed on the top surface, with a *p-i-n* diode and a varactor diode bridging the gaps between segments. The *p-i-n* diode functions as a current-controlled variable *RC* circuit under forward bias, while the varactor diode provides voltage-controlled capacitance under

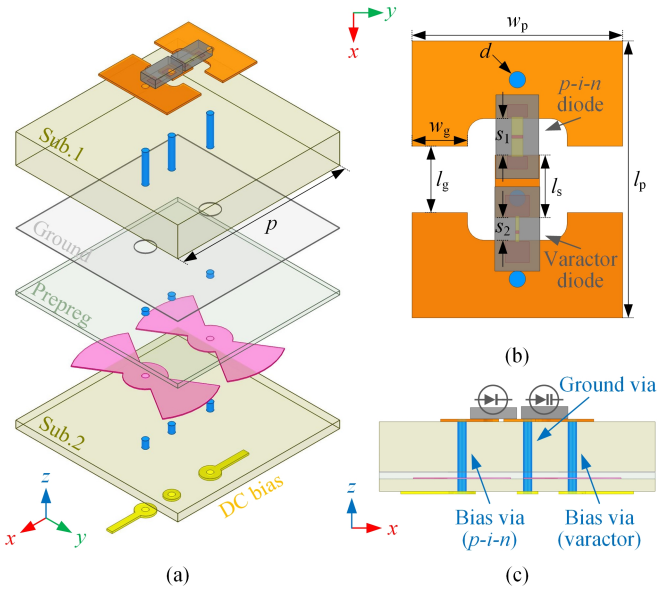

Figure 3.1: Configuration of the mmWave UC featuring two vertical loops embedded within a segmented, end-folded patch, integrating a *p-i-n* diode and a varactor diode. (a) Exploded view. (b) Top view. (c) Side view.

reverse bias. This dual-diode configuration enables independent amplitude-phase control over a wide tuning range. Three plated vias connect the patch segments to facilitate independent diode biasing. Two bias vias, located at the folded segments, are linked to radial stubs serving as RF chokes. Additionally, the inclusion of these vias transforms the planar patch into two vertically-placed coupled loops.

3.2 Γ-Coverage and Performance Metrics

The UC design follows a combined EM-circuit co-simulation approach using Ansys HFSS and Keysight ADS. A full-wave EM model is constructed in HFSS with sidewall periodic boundaries and a Floquet port above the UC aperture. To reduce computational effort, a differential lumped port replaces the lumped *RLC* boundary in the EMM. Circuit-level diode switching is then

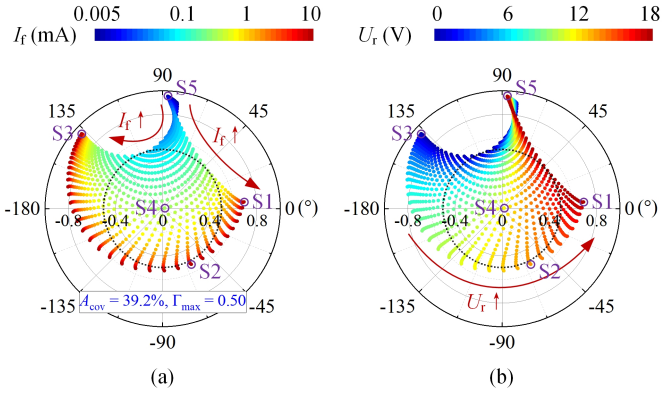

Figure 3.2: Simulated Γ-coverage under normal PW incidence at 28 GHz. The dot locations are identical, with color scale indicating (a) I_f and (b) U_r.

handled in ADS by terminating the differential ports with varying junction impedances. In this way, Γ is obtained by sweeping all combinations of I_f (5 μA to 10 mA, 41 logarithmic steps) and U_r (0 V to 18 V, 37 linear steps).

To characterize the UC's reflection response over a wide bias range and assess the amplitude-phase interaction, a generalized complex-plane representation, referred to as Γ-coverage, is introduced. For the x-polarized controllable component, the Γ-coverage under normal PW incidence at 28 GHz is shown in Fig. 3.2. This plot visualizes the set of all complex-valued Γ associated with various bias states, offering an intuitive view of the amplitude-phase tuning capabilities. Unlike traditional Cartesian representations that separately display amplitude and phase, the Γ-coverage maps each bias state directly to a unique point on the complex plane, capturing the joint influence of the *p-i-n* and varactor diodes. Independent amplitude-phase control is thus achieved by selecting appropriate combinations of diode bias states from the Γ-coverage.

The proposed Γ-coverage provides a universal framework for evaluating reconfigurability. Two key performance metrics are defined to quantify the UC's amplitude-phase tunability from complementary perspectives:

1) Relative Γ-coverage area (A_{cov}): Defined as the ratio of the Γ-coverage area to the area of the unit circle (i.e., π). It quantifies the overall controllable amplitude-phase space of the UC.

2) Maximum amplitude for full 360° phase control (Γ_{max}): Defined as the

radius of the largest circle fully enclosed within the Γ-coverage. Inside this region, the UC supports complete phase tuning from $-180°$ to $+180°$, with amplitude control ranging from 0 to $\Gamma_{\max}$.

The proposed UC particularly suited for OTA testing applications, where large Γ-coverage is essential. As shown in Fig. 3.2 at 28 GHz, the design achieves $\Gamma_{\max} = 0.5$ and $A_{\text{cov}} = 39.2\%$.

3.3 Semi-Analytical ECM of the UC

In this section, a semi-analytical UC ECM is developed by combining Floquet modal expansion with lumped component modeling. The analysis begins with modal source decomposition into TE_{mn} and TM_{mn} types. Fig. 3.3 illustrates the proposed ECM considering the dominant Floquet modes (i.e., $m = n = 0$).

At the air-dielectric interface ($z = 0$), the admittance seen when looking upward from line $\overline{AB}$ corresponds to the equivalent surface admittance contributed by all other Floquet modes and tunable components. This admittance is scaled by a transformer with turns ratio N for the mode of interest. The grounded dielectric slab in $z < 0$ is modeled as a short-circuited transmission line with input admittance $Y_{\text{sub},mn}^{\text{TE|TM}}$, while the incident PW in $z > 0$ is represented by an input port with wave admittance $Y_{\text{s},mn}^{\text{TE|TM}}$; both are functions of the incidence angles (θ, φ).

This formulation allows for an analytical solution to the ECM. However, the equivalent admittance above $\overline{AB}$ highly depends on the UC's current distribution. While closed-form solutions are available for regular geometries, they are generally inapplicable to the complex layouts of practical UCs. Therefore, a lumped *RLC* equivalent circuit is adopted as a more practical alternative.

The DCMs in Chapter 2 are integrated into the ECM. The two end-folded patch segments are modeled as *RLC* series resonators. Due to slight asymmetry in the diode pad dimensions, the current path on the *p-i-n* diode side is longer, imposing the constraint $L_1 > L_2$. Both segments share the same capacitance C_1, representing their charge storage and mutual coupling with adjacent UCs. The resistance R stands for ohmic loss. Moreover, the ground and bias vias supporting vertical current flow are modeled as self partial inductances L_3 and L_4, with $L_3 < L_4$ due to the longer path of the bias vias connected to the radial stubs. The stubs behave as large distributed capacitors, shorting the bias vias at mmWave frequencies and forming two vertical

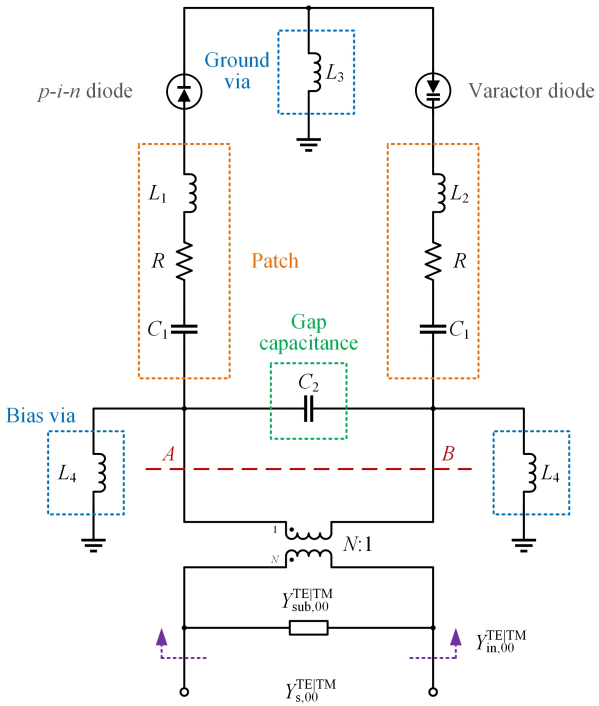

Figure 3.3: Schematic of the semi-analytical UC ECM, combining Floquet modal expansion with lumped component modeling.

current loops. Additionally, the folded patch ends introduce microstrip discontinuities, modeled as gap capacitances C_g. Two such gaps in parallel yield a total capacitance $C_2 = 2C_g$, enhancing coupling between the segments.

Circuit simulations are conducted to validate the ECM. The resulting A_{cov} distributions in Fig. 3.4 exhibit strong agreement with those obtained from EM-circuit co-simulations, particularly in the $\varphi = 90°$ plane. The model is considered valid for $\theta \in [-40°, 40°]$ in the $\varphi = 0°$ plane and $\theta \in [-60°, 60°]$ in the $\varphi = 90°$ plane. The observed φ-plane deviations at larger θ are primarily attributed to the x-polarized, non-rotationally symmetric UC geometry.

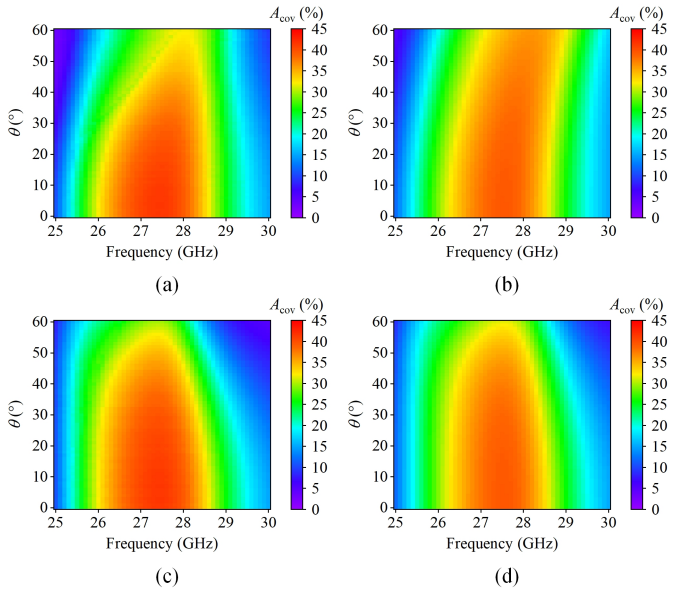

Figure 3.4: Simulated A_{cov} distributions versus incident angle and frequency. (a), (b) Results based on EM-circuit co-simulation and ECM in the $\varphi = 0°$ plane. (c), (d) Corresponding results in the $\varphi = 90°$ plane.

3.4 Measurement Results

To experimentally validate the UC, this section employs a cost-effective waveguide simulator technique to emulate an infinite array under frequency-specific, oblique quasi-PW incidence. As shown in Fig. 3.5, a 1 × 2 UC prototype is mounted at one end of a custom CNC-machined brass waveguide, with the aperture precisely matching the dimensions of two UCs. The opposite end interfaces with a standard WR-28 waveguide via a quarter-wavelength transformer and connects to a coaxial adapter for measurement. TRL calibration is performed using a back-to-back two-port reference. The PCB is supported by a metal base to ensure structural stability. Edge vias enclosing the UCs form electric sidewalls. The diodes are manually soldered, and the bias lines are routed to a six-position surface-mount socket. Bias voltages and currents are supplied via digital-to-analog converters and cascaded voltage-to-current converters, enabling 16-bit high-resolution tuning of both amplitude and phase.

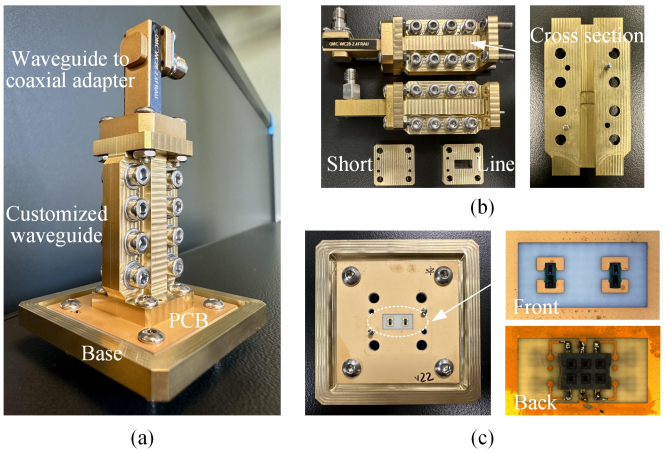

Figure 3.5: Experimental setup for UC characterization. (a) Waveguide simulator. (b) TRL calibration kit. (c) PCB prototype with 1 × 2 UCs.

Fig. 3.6 compares the simulated and measured Γ-coverage at various frequencies. The measured Γ distributions closely match the simulations, exhibiting consistent rotational trends across frequencies, with only minor discrepancies at higher frequencies. Compared to the simulations, the measured values of A_{cov} and Γ_{max} are slightly reduced, as evidenced by the contracted boundaries of the Γ-coverage plots. Further experimental investigation attributes this discrepancy primarily to practical non-idealities, including copper surface roughness, diode mounting materials, and PCB surface finishes. These factors become increasingly significant at mmWave frequencies and collectively contribute to the observed performance degradation.

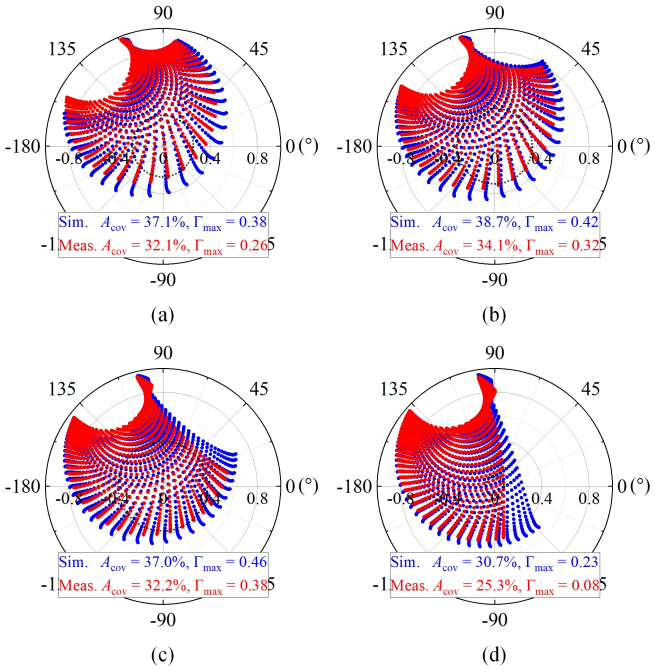

Figure 3.6: Simulated (blue dots) and measured (red dots) Γ-coverage. (a) 26.5 GHz. (b) 27 GHz. (c) 27.5 GHz. (d) 28 GHz.

CHAPTER 4

Exemplification for OTA Testing

Despite the reflection loss associated with a reduced $\Gamma_{\max}$, the proposed design remains promising for OTA testing applications. Unlike communication systems where signal-to-noise ratio dominates system performance, OTA testing scenarios prioritize fine-resolution amplitude and phase control. In such environments, RIS-induced losses can be calibrated and compensated during testing, with the main trade-off being a slightly reduced measurement dynamic range. This makes the proposed UC particularly appropriate for OTA testing applications, where moderate reflection loss is tolerable.

To highlight its practical potential, this chapter applies the RIS UC developed in Chaper 3 to a typical OTA scenario as an RIS-assisted PW generator, serving as a CATR while enabling tunable PW arrival angles without the need for mechanical rotation. Further details can be found in Paper [C]. The test configuration includes a 21 $\times$ 21-UC RIS illuminated by a 9 dBi pyramidal horn, targeting an 11 $\times$ 11 bow-tie DUT with a 22.8 dBi gain. The objective is to synthesis a PW with amplitude and phase errors below 1 dB and 10°, respectively, within the designated test zone.

Fig. 4.1 illustrates the simulation setup. The RIS is configured in diverse UC states with optimal Γ values, ranging from near-full absorption ($|\Gamma^{x,x}| <$

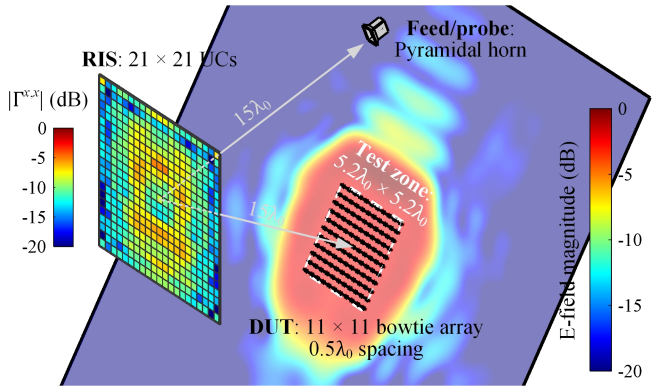

Figure 4.1: Simulated setup for RIS-assisted near-field PW generation at 28 GHz.

-20 dB at RIS edges) to high reflection ($|\Gamma^{x,x}| \approx -6$ dB at the center). Both the feed-to-RIS and RIS-to-DUT distances are set to $15\lambda_0$ (about 0.16 m). The simulated electric field errors across the DUT aperture remain within 0.6 dB in amplitude and 2.5° in phase, indicating high-uniformity PW synthesis. The simulated transmission loss from feed to DUT via the RIS is 27.6 dB.

For comparison, achieving the same 2.5° phase error in an equivalent far-field setup would require a much larger probe-to-DUT distance of $991\lambda_0$ (about 10.62 m), incurring considerably higher signal attenuation. The calculated free-space path loss using the Friis transmission formula amounts to 50.4 dB. Therefore, the OTA setup employing the proposed RIS UC achieves a 22.8 dB reduction in system loss relative to the conventional far-field test range. This confirms that the moderate intrinsic loss of the UC has negligible impact in RIS-based CATR systems, which benefit from significantly improved measurement dynamic range and physical compactness.

CHAPTER 5

Summary of Included Papers

This chapter provides a summary of the included papers.

5.1 Paper A

Y. Zhu, A. R. Vilenskiy, O. A. Iupikov, P. S. Krasov, T. Emanuelsson, G. Lasser, M. V. Ivashina
A varactor-based reconfigurable intelligent surface concept for 5G/6G mm-wave applications
2024 18th European Conference on Antennas and Propagation (EuCAP), Glasgow, United Kingdom, pp. 1–5, 2024.
 DOI: 10.23919/EuCAP60739.2024.10501072.

A varactor-based reconfigurable intelligent surface (RIS) concept is presented for low-cost, high-precision beamforming of 5G/6G mm-waves. To enable this, we maximize the RIS unit cell (UC) phase coverage by (i) employing a varactor diode-tuned slotted-patch UC, and (ii) adding a metallic loop and via fence across the UC boundary, which also improves the bandwidth and angular insensitivity. In an infinite RIS environment, the UC exhibits a phase

coverage of 330.7 degrees while maintaining the insensitivity of reflection coefficients up to 50-degree elevation angle. This UC design demonstrates a phase coverage that exceeds 315 degrees with under 0.7-dB reflection loss across a 11.6% bandwidth, where the capacitance tuning ratio of the considered commercial off-the-shelf varactor diode is only 1.8. A 15 × 15 RIS model with a 3-bit phase quantization is used for beam steering performance validation; it predicts the realized gain of 19.5 dBi for the 30-degree beam-steering direction at 28 GHz.

5.2 Paper B

Y. Zhu, A. Vilenskiy, O. Iupikov, P. Krasov, T. Emanuelsson, G. Lasser, M. Ivashina
Improved equivalent circuit model of p-i-n diodes for amplitude and phase controllable mmWave reconfigurable intelligent surfaces
2024 IEEE International Symposium on Antennas and Propagation and INC/USNC-URSI Radio Science Meeting (AP-S/INC-USNC-URSI), Firenze, Italy, pp. 1583–1584, 2024.
 DOI: 10.1109/AP-S/INC-USNC-URSI52054.2024.10686865.

An improved equivalent circuit model (ECM) of *p-i-n* diodes is developed and applied to amplitude and phase controllable mmWave reconfigurable intelligent surfaces (RISs). The proposed ECM takes into account the variable junction resistance and capacitance of forward-biased *p-i-n* diodes in the transition state (instead of a conventional simplified resistance model) that is critical at mmWave frequencies. The flip-chip AlGaAs *p-i-n* diodes have been characterized in a 2-port coplanar measurement setup. Both the improved ECM and the electromagnetic model are constructed and validated. The ECM is used for a 28-GHz RIS design with amplitude and phase control of the reflection coefficient. The observed non-linear performance combined with an additional phase shift of up to 84° introduced by the variable junction capacitance indicates the value of the proposed model.

5.3 Paper C

Y. Zhu, A. R. Vilenskiy, O. A. Iupikov, P. S. Krasov, T. Emanuelsson, G. Lasser, M. V. Ivashina
Millimeter-wave reconfigurable intelligent surface with independent and continuous amplitude-phase control: Unit cell design and circuit model
IEEE Transactions on Antennas and Propagation,
early access.
 DOI: 10.1109/TAP.2025.3577744.

This paper presents a reconfigurable intelligent surface (RIS) unit cell (UC) with independent amplitude-phase control, crucial for complex field shaping in RIS-assisted over-the-air testing. Unlike conventional phase-only tuning UCs, the proposed design enables continuous control from reflective to absorptive states for advanced field synthesis. To quantify reconfigurability, we introduce a generalized complex-plane representation, termed Γ-coverage, mapping both amplitude and phase over all bias states. For the first time at millimeter-wave frequencies, a loop-embedded end-folded UC integrating a forward-biased *p-i-n* diode and a reverse-biased varactor diode is developed to maximize Γ-coverage. The UC achieves a 0–0.5 amplitude tuning range (equivalent to a controllable loss from complete attenuation to 6 dB) and a $-180°$–$+180°$ phase tuning range at 28 GHz. The maximum incident angle reaches 45° within ±48° phase fluctuations, extending to 60° with full-phase tuning under a 12 dB loss criterion. We derive empirical circuit models for both diodes to account for high-frequency parasitic effects and formulate a semi-analytical UC equivalent circuit model. The UC prototype is evaluated using a waveguide simulator. The operational bandwidths for reconfigurability are 25.8–28.0 GHz with a relative Γ-coverage area exceeding 25%, and 26.5–27.7 GHz for 360° phase control with 8.4–12 dB losses. The instantaneous bandwidth for stable operation spans 27.3–27.7 GHz, maintaining ±50° phase fluctuations within 5.6–13.4 dB losses. The UC is analyzed in an RIS-assisted near-field plane-wave generation scenario for a compact antenna test range (CATR), achieving high field uniformity (< 0.6 dB and $< 2.5°$ errors). Despite intrinsic UC losses, the RIS-based CATR reduces total system loss by 22.8 dB compared to a far-field test range.

CHAPTER 6

Concluding Remarks and Future Work

This thesis investigates unconventional RIS functionality that enables simultaneous, independent, and continuous amplitude-phase control, with a focus on OTA testing of wireless systems. Through a systematic exploration of tunable components, modeling and analysis methodologies, and practical UC implementation strategies, the work contributes to the advancement of amplitude-phase controllable RIS technology at high frequencies, particularly within the K_a-band. The demonstration of the proposed RIS in OTA testing scenarios confirms the suitability of mmWave RISs for manipulating EM environments to achieve complex field shaping. This thesis establishes a solid foundation for the development and deployment of mmWave RISs in OTA testing, paving the way for their integration into future wireless systems and metrology platforms.

Several promising directions may further extend this research:

RIS UC performance improvement Although the developed RIS UC achieves an amplitude tuning range of 0–0.5 and a full 360° phase tuning range, inherent losses at mmWave frequencies constrain the expansion of Γ-coverage, and the frequency dependence of Γ-coverage presents challenges to wideband operation. Overcoming these limitations calls for further investigation into

advanced UC configurations, as well as novel tunable materials and device technologies. Moreover, incorporating an extra control dimension, such as implementing dual-polarized RIS UCs, could significantly enhance applicability in wireless systems, albeit at the cost of increased design complexity. Tackling these challenges will not only broaden the application prospects of RISs in OTA testing but also boost their potential for wider deployment in next-generation wireless communications and related fields (e.g., absorptive RISs for jammer mitigation as presented in Paper [E]).

System-level RIS validation Preliminary simulations of the RIS-based CATR suggest clear advantages over conventional far-field test ranges. However, full system-level development and experimental validation with a dedicated testbed demonstrator are essential to assess real-world performance. Accurate RIS panel modeling must holistically account for factors such as modular sub-array structures, inter-UC mutual coupling, array edge diffraction and truncation, as well as biasing circuitry layout, including interconnects and control board architecture. Achieving precise control of *p-i-n* diode currents also remains a technical hurdle. Furthermore, robust calibration and measurement methodologies are crucial to validate RIS performance in representative OTA testing scenarios. Our ongoing research addresses several critical aspects that remain underexplored in the literature, including: an OTA back-scattering approach for recovering Γ, while accounting for coupling effects between the tunable electronics and the passive reflective UC structure (see Paper [H]); RIS functional testing methods for diagnostic purposes (see Paper [I]); and monostatic RIS characterization techniques incorporating time gating to suppress unwanted reflections in the measurement setup (see Paper [J]). Such efforts are key to exploiting the full potential of RIS technology in future time- and cost-efficient OTA platforms.

References

[1] M. D. Renzo, A. Zappone, M. Debbah, *et al.*, "Smart radio environments empowered by reconfigurable intelligent surfaces: How it works, state of research, and the road ahead," *IEEE J. Sel. Areas Commun.*, vol. 38, no. 11, pp. 2450–2525, 2020.

[2] Y. Jiang, F. Gao, M. Jian, S. Zhang, and W. Zhang, "Reconfigurable intelligent surface for near field communications: Beamforming and sensing," *IEEE Trans. Wireless Commun.*, vol. 22, no. 5, pp. 3447–3459, 2023.

[3] Y. Feng, Q. Hu, K. Qu, W. Yang, Y. Zheng, and K. Chen, "Reconfigurable intelligent surfaces: Design, implementation, and practical demonstration," *Electromagn. Sci.*, vol. 1, no. 2, pp. 1–21, 2023.

[4] J. Liao, S. Guo, L. Yuan, C. Ji, C. Huang, and X. Luo, "Independent manipulation of reflection amplitude and phase by a single-layer reconfigurable metasurface," *Adv. Opt. Mater.*, vol. 10, no. 4, 2022, Art. no. 2101551.

[5] H. L. Wang, Y. K. Zhang, T. Y. Zhang, H. F. Ma, and T. J. Cui, "Broadband and programmable amplitude-phase-joint-coding information metasurface," *ACS Appl. Mater. & Interfaces*, vol. 14, no. 25, pp. 29 431–29 440, 2022.

[6] J. C. Liang, L. Zhang, Z. W. Cheng, P. Zhang, and T. J. Cui, "Flexible beam manipulations by reconfigurable intelligent surface with indepen-

dent control of amplitude and phase," *Front. Mater.*, vol. 9, 2022, Art. no. 946163.

[7] H. P. Wang, Y. B. Li, H. Li, *et al.*, "Intelligent metasurface with frequency recognition for adaptive manipulation of electromagnetic wave," *Nanophotonics*, vol. 11, no. 7, pp. 1401–1411, 2022.

[8] Q. Xiong, Z. Zhang, X. Ma, *et al.*, "Multi-channel wireless communication based on amplitude-phase reconfigurable space-coding beamforming metasurface," *Adv. Electron. Mater.*, vol. 10, no. 8, 2024, Art. no. 2400056.

[9] R. Phon, M. Lee, C. Lor, and S. Lim, "Multifunctional reflective metasurface to independently and simultaneously control amplitude and phase with frequency tunability," *Adv. Opt. Mater.*, vol. 11, no. 14, 2023, Art. no. 2202943.

[10] M. K. Emara, D. Kundu, K. Macdonell, L. M. Rufail, and S. Gupta, "Dynamic metasurface reflectors based on coupled resonators for simultaneous magnitude and phase control," *IEEE Access*, vol. 11, pp. 129 552–129 565, 2023.

[11] Y. H. Liu, S. Y. Wang, K. N. Qi, and Y. B. Li, "Dynamic controlling the bistatic RCS by programmable metasurface with continuous and independent manipulation of reflective phase and amplitude," *IEEE Antennas Wireless Propag. Lett.*, vol. 23, no. 3, pp. 1000–1004, 2024.

[12] J. Zhang, X. Wei, I. D. Rukhlenko, H.-T. Chen, and W. Zhu, "Electrically tunable metasurface with independent frequency and amplitude modulations," *ACS Photon.*, vol. 7, no. 1, pp. 265–271, 2019.

[13] C. Huang, J. Liao, C. Ji, J. Peng, L. Yuan, and X. Luo, "Graphene-integrated reconfigurable metasurface for independent manipulation of reflection magnitude and phase," *Adv. Opt. Mater.*, vol. 9, no. 7, 2021, Art. no. 2001950.

[14] J. Shabanpour, S. Beyraghi, and C. R. Simovski, "THz multiple-beam manipulation by reconfigurable intelligent surface with independent phase/amplitude control," in *Proc. 17th Int. Congr. Artif. Mater. Novel Wave Phenomena*, 2023, pp. 338–340.

[15] K. M. Kossifos, J. Georgiou, and M. A. Antoniades, "ASIC-enabled programmable metasurfaces—Part 1: Design and characterization," *IEEE Trans. Antennas Propag.*, vol. 72, no. 3, pp. 2790–2799, 2024.

[16] J.-M. Baracco, P. Ratajczak, P. Brachat, J.-M. Fargeas, and G. Toso, "Ka-band reconfigurable reflectarrays using varactor technology for space applications: A proposed design," *IEEE Antennas Propag. Mag.*, vol. 64, no. 1, pp. 27–38, 2022.

[17] R. Wang, Y. Yang, B. Makki, and A. Shamim, "A wideband reconfigurable intelligent surface for 5G millimeter-wave applications," *IEEE Trans. Antennas Propag.*, vol. 72, no. 3, pp. 2399–2410, 2024.

[18] E. Wang, G. Peng, K. Zhong, *et al.*, "A 1296-cell reconfigurable reflectarray antenna with 2-bit phase resolution for Ka-band applications," *IEEE Trans. Antennas Propag.*, vol. 72, no. 4, pp. 3425–3437, 2024.

[19] MACOM. "Varactor tuning diodes." (2023), [Online]. Available: `https://www.macom.com/products/rf-microwave-mmwave/diodes/varactor-tuning-diodes` (visited on 10/02/2023).

[20] S. V. Hum and B. Du, "Equivalent circuit modeling for reflectarrays using Floquet modal expansion," *IEEE Trans. Antennas Propag.*, vol. 65, no. 3, pp. 1131–1140, 2017.

[21] E. Baladi and S. V. Hum, "Equivalent circuit models for metasurfaces using Floquet modal expansion of surface current distributions," *IEEE Trans. Antennas Propag.*, vol. 69, no. 9, pp. 5691–5703, 2021.